Evolutions of magnetized and rotating neutron stars

Steven L. Liebling,[1] Luis Lehner,[2,3,4] David Neilsen,[5] and Carlos Palenzuela[6,7]

[1]*Department of Physics, Long Island University–C.W. Post Campus, Brookville, New York 11548, USA*
[2]*Perimeter Institute for Theoretical Physics, Waterloo, Ontario, Canada N2L 2Y5*
[3]*Department of Physics, University of Guelph, Guelph, Ontario, Canada N1G 2W1*
[4]*Canadian Institute for Advanced Research, Cosmology & Gravity Program, Toronto, Ontario, Canada*
[5]*Department of Physics and Astronomy, Brigham Young University, Provo, Utah 84602, USA*
[6]*Canadian Institute for Theoretical Astrophysics (CITA), Toronto, Ontario, Canada M5S 3H8*
[7]*Max Planck Institut for Gravitational Physics, Albert Einstein Institute, Am Muhlenberg 1, D-14476 Golm, Germany*
(Received 5 January 2010; published 9 June 2010)

We study the evolution of magnetized and rigidly rotating neutron stars within a fully general relativistic implementation of ideal magnetohydrodynamics with no assumed symmetries in three spatial dimensions. The stars are modeled as rotating, magnetized polytropic stars, and we examine diverse scenarios to study their dynamics and stability properties. In particular, we concentrate on the stability of the stars and possible critical behavior. In addition to their intrinsic physical significance, we use these evolutions as further tests of our implementation, which incorporates new developments to handle magnetized systems.

I. INTRODUCTION

Neutron stars play a key role in some of the most interesting astrophysical events observed, from supernova remnants and pulsars to a less certain role in long gamma ray bursts. As such they have attracted significant research into their dynamics (for a recent review see [1]). In this paper, we revisit the dynamics of rotating, and possibly magnetized, neutron stars modeled as polytropic stars within a fully nonlinear, general relativistic model of ideal magnetohydrodynamics (GR + MHD). We study the stability properties of these stars and highlight possible critical behavior exhibited by the system. Furthermore, our studies serve to demonstrate the effectiveness of our code and certain new developments discussed here. This code has been applied to other astrophysical problems [2–7].

In recent years, a number of fully relativistic evolutions (as opposed to those using Newtonian gravity or other approximations to general relativity) of rotating polytropes have appeared studying gravitational wave production and black hole formation in astrophysically relevant systems. To this end, studies beyond spherical symmetry are required, which are computationally more demanding. For instance, rotating stars require moving beyond spherical symmetry and many interesting axisymmetric scenarios can be addressed using 2D implementations allowing for excellent resolution without requiring major resources (e.g. [8–10]). In contrast, studies of the most general flows and instabilities require 3D simulations and are the most expensive realistically accessible scenarios being currently considered. Future efforts, including radiation transport mechanisms, will move beyond 3D scenarios and require efficient use of petaflop (and beyond) resources (e.g. [11]).

Another important distinction in these studies is whether the modeled stars are rigidly rotating or allow for differential rotation. Rigidly rotating stars support more mass than nonrotating ones (so-called TOV stars), but generally do not support the largest masses achieved with differential rotation nor do they demonstrate some of the more interesting instabilities such as the bar mode instability [12]. Instead, uniformly rotating stars tend to demonstrate one of two behaviors: stability or instability to collapse to a black hole. Previous studies suggest that significant disks do not form from such collapse [13–15]. Recall that stars rotating differentially are expected to settle into rigidly rotating configurations on short time scales, and hence a normal neutron star observed today is generally expected to be rigidly rotating.

Achieving ever more realism, models of neutron stars have also begun to consider stars with magnetic field [9,16–18]. Magnetic fields provide, in particular, an effective pressure that generally supports greater mass [19] as well as an efficient way to transport angular momentum. In differentially rotating stars, even small magnetic fields can be amplified by the magnetorotational instability. Generally these studies begin with a nonmagnetized neutron star to which a small, seed magnetic field is added. However, in [20], fully consistent, magnetized stars are evolved, although only nonrotating results are presented. Another approach is to study the modes through a perturbation approach [21,22] and analyze the growth of these modes with respect to a given stationary solution. The dynamical behavior of magnetized stars is important also for their role in explaining strong electromagnetic emissions. Indeed, isolated stars with strong magnetic fields, so-called *magnetars*, are suspected to be the engines powering

anomalous x-ray pulsars and soft gamma ray repeaters [23]. At least 10% of all neutron stars [24] are born as magnetars. In the context of single stars, it is thus interesting to examine whether strong magnetic fields may deform stars away from axisymmetry making them strong producers of gravitational waves [25].

Here we present results with uniformly rotating neutron stars that possess a fully consistent magnetic dipole moment. That is to say, the initial data used here represents a stationary state of the full GR + MHD equations. These evolutions are computed with a general relativity code employing the generalized harmonic scheme (allowing for black hole excision). Further, no symmetry assumptions are made. High resolutions are achieved using a distributed adaptive mesh refinement infrastructure. These evolutions demonstrate that our code can evolve a stable rotating star for many periods accurately. Similarly, unstable stars evolve to black holes with no evidence of any significant disk forming. Finally, we give evidence that unstable, rotating, magnetized stars represent minimally unstable solutions that could serve as type I critical solutions.

In Sec. II we provide details about the formulation of the equations. In Sec. III we discuss aspects of our numerical implementation and describe the diagnostic quantities evaluated in Sec. IV. In Sec. V we discuss the initial data we use. We present our results in Sec. VI and conclude in Sec. VII.

II. FORMULATION AND EQUATIONS OF MOTION

Neutron stars can be modeled by relativistic fluids (possibly with the inclusion of magnetic fields) under the action of strong gravitational fields [26]. These systems are governed both by the Einstein equations for the geometry and by the relativistic equations of magnetohydrodynamics for the matter. We write both systems as first-order hyperbolic equations. This form of the equations is convenient in order to take advantage of several rigorous numerical techniques devised for such systems to ensure, at the linear level, stability of the implementation. More information regarding the motivation for this approach can be found in [2,27,28]. By way of notation, we use letters from the beginning of the alphabet (a, b, c) for spacetime indices, while letters from the middle of the alphabet (i, j, k) range over spatial components. We adopt geometric units where $c = G = 1$. However, as discussed in Sec. III, when appropriate, we rescale the value of G to achieve improved accuracy in the conservative to primitive variable conversion stage.

A. The Einstein equations

The Einstein equations can be written as a system of ten nonlinear partial differential equations for the spacetime metric g_{ab}. The harmonic formulation of the Einstein equations exploits the fact that the coordinates x^a can be chosen satisfying the generalized harmonic condition [29,30]

$$\nabla^c \nabla_c x^a = -\Gamma_a = H^a(t, x^i), \tag{1}$$

where $\Gamma^a \equiv g^{bc}\Gamma_{abc}$ are the contracted Christoffel symbols. The arbitrary source functions $H^a(t, x^i)$ determine the coordinate freedom of Einstein equations. The original harmonic coordinates correspond to the case $H^a(t, x^i) = 0$, which is the choice here. The Einstein equations can be expressed in their generalized harmonic form [29], in particular,

$$g^{cd}\partial_{cd}g_{ab} + \partial_a H_b + \partial_b H_a$$
$$= -16\pi\left(T_{ab} - \frac{T}{2}g_{ab}\right) + 2\Gamma_{cab}H^c$$
$$+ 2g^{cd}g^{ef}(\partial_e g_{ac}\partial_f g_{bd} - \Gamma_{ace}\Gamma_{bdf}). \tag{2}$$

The matter is coupled to the geometry by means of the stress-energy tensor T_{ab} and its trace $T \equiv g^{ab}T_{ab}$, which will be dictated by the particular model of magnetized fluid under consideration, detailed in the next subsection.

The spacetime can be foliated into hypersurfaces of constant coordinate time $x^0 \equiv t = $ const. On these spacelike hypersurfaces, one defines a spatial 3-metric $h_{ij} = g_{ij}$. A vector normal to the hypersurfaces is given by $n_a \equiv -\nabla_a t/\|\nabla_a t\|$, and coordinates defined on neighboring hypersurfaces can be related through the lapse, α, and shift vector, β^i. With these definitions, the spacetime differential element can then be written as

$$ds^2 = g_{ab}dx^a dx^b$$
$$= -\alpha^2 dt^2 + h_{ij}(dx^i + \beta^i dt)(dx^j + \beta^j dt). \tag{3}$$

Indices on spacetime quantities are raised and lowered with the 4-metric, g_{ab}, and its inverse, while the 3-metric h_{ij} and its inverse are used to raise and lower indices on spatial quantities.

We adopt a first-order reduction of the second order differential equations represented in Eqs. (2). This reduction can be achieved by introducing new independent variables related to the time and space derivatives of the fields

$$Q_{ab} \equiv -n^c\partial_c g_{ab}, \qquad D_{iab} \equiv \partial_i g_{ab}. \tag{4}$$

Within these definitions we can write our evolution equations in our GH formalism in the following way [31]:

$$\partial_t g_{ab} = \beta^k D_{kab} - \alpha Q_{ab}, \tag{5}$$

$$\partial_t Q_{ab} = \beta^k \partial_k Q_{ab} - \alpha h^{ij} \partial_i D_{jab} - \alpha \partial_a H_b - \alpha \partial_b H_a + 2\alpha \Gamma_{cab} H^c + 2\alpha g^{cd}(h^{ij} D_{ica} D_{jdb} - Q_{ca} Q_{db} - g^{ef} \Gamma_{ace} \Gamma_{bdf})$$
$$- \frac{\alpha}{2} n^c n^d Q_{cd} Q_{ab} - \alpha h^{ij} D_{iab} Q_{jc} n^c - 8\pi\alpha(2T_{ab} - g_{ab}T) - 2\sigma_0 \alpha [n_a Z_b + n_b Z_a - g_{ab} n^c Z_c]$$
$$+ \sigma_1 \beta^i (D_{iab} - \partial_i g_{ab}), \tag{6}$$

$$\partial_t D_{iab} = \beta^k \partial_k D_{iab} - \alpha \partial_i Q_{ab} + \frac{\alpha}{2} n^c n^d D_{icd} Q_{ab} + \alpha h^{jk} n^c D_{ijc} D_{kab} - \sigma_1 \alpha(D_{iab} - \partial_i g_{ab}). \tag{7}$$

This GH formulation includes a number of constraints that must be satisfied for consistency. On the one hand, there are two sets of first-order constraints, obtained from Eqs. (4) and defined as

$$\mathcal{C}_{iab} \equiv \partial_i g_{ab} - D_{iab} = 0,$$
$$\mathcal{C}_{ijab} \equiv \partial_i D_{jab} - \partial_j D_{iab} = 0, \tag{8}$$

which were introduced when performing the reduction to first-order [2,31]. On the other hand, there are the Hamiltonian and momentum constraints that in the generalized harmonic formulation show up in terms of a four-vector Z_a, which is defined as

$$2Z^a \equiv -\Gamma_a - H^a(t, x^i). \tag{9}$$

It can be shown that the Hamiltonian and momentum constraints are satisfied if $Z^a = \partial_t Z^a = 0$ [32]. In order to dynamically control the violation of the constraints, we have included certain terms proportional to these constraints (8) and (9). These additional terms depend on free parameters σ_0 and σ_1, allowing one to dynamically damp constraint—including the Hamiltonian, momentum, and first-order constraints (8)—violating modes on a time scale proportional to $-\sigma_i$ [31,33].

We evolve the gravitational field equations shown in Eqs. (5)–(7). These equations rely on the computation of the four-dimensional Christoffel symbols from the metric g_{ab}

$$\Gamma_{abc} = \tfrac{1}{2}(D_{bca} + D_{cba} - D_{abc}). \tag{10}$$

While we evolve the D_{iab} functions, the set D_{0ab} are not evolved, but are calculated from evolved quantities as

$$D_{0ab} = -\alpha Q_{ab} + \beta^k D_{kab}. \tag{11}$$

This description suffices to explain the gravitational evolution, and the following section describes the evolution of the matter. However, we note here that the MHD equations are written in the standard $3 + 1$ decomposition of spacetime and thus require the spatial metric h_{ij}, the lapse α, shift β^i, and Arnowitt-Deser-Misner (ADM) extrinsic curvature, K_{ij}. These quantities can be written in terms of our evolved fields using

$$h_{ij} = g_{ij}, \qquad \alpha = \sqrt{-1/g^{00}}, \qquad \beta^i = \gamma^{ij} g_{0j},$$
$$K_{ij} = \frac{1}{2} Q_{ij} + \frac{1}{\alpha}(D_{(ij)0} - \beta^k D_{(ij)k}). \tag{12}$$

Conversely, the Hamiltonian and momentum constraints are usually written in terms of spatial derivatives of the metric D_{kij} and the extrinsic curvature K_{ij}. In fact, we use these $3 + 1$ quantities (and similar expressions for their derivatives) to calculate the residuals of the Hamiltonian and momentum constraints expressed in their standard form.

B. MHD equations

We now briefly introduce the perfect fluid equations. Additional information can be found in our previous work [27,28] as well as in topical review articles [34,35].

The stress-energy tensor for the perfect fluid in the presence of a Maxwell field is given by

$$T_{ab} = [\rho_o(1 + \epsilon) + P]u_a u_b + P g_{ab} + F_a{}^c F_{bc}$$
$$- \tfrac{1}{4} g_{ab} F^{cd} F_{cd}. \tag{13}$$

The fluid is described by rest mass density ρ_o, the specific internal energy density ϵ, the isotropic pressure P, and the four velocity of the fluid u^a. With these quantities we can construct the enthalpy

$$h_e = \rho_o + \rho_o \epsilon + P \tag{14}$$

and construct the standard spatial coordinate velocity of the fluid v^i as

$$W \equiv -n^a u_a, \qquad v^i \equiv \frac{1}{W} h^i{}_j u^j, \tag{15}$$

where W is the Lorentz factor between the fluid frame and the fiducial ADM observers.

The Maxwell tensor F_{ab} can be written as

$$F^{ab} = n^a E^b - n^b E^a + \epsilon^{abcd} B_c n_d, \tag{16}$$

where E^a and B^a are the electric and magnetic fields measured by a "normal" observer n^a. Consequently, both fields are purely spatial, i.e., $E^a n_a = B^a n_a = 0$.

The evolution of the magnetized fluid is described by different sets of conservation laws. The magnetic field, in the ideal MHD limit, follows the Maxwell equation

$$\nabla_\mu(^*F^{\mu\nu} + g^{\mu\nu}\Psi) = \kappa n^\nu \Psi, \tag{17}$$

where $^*F^{ab} \equiv \epsilon^{abcd} F_{cd}/2$ is the dual of the Maxwell tensor and we have introduced a real scalar field Ψ to control the divergence constraint. This technique is known as divergence cleaning [36] and allows for a convenient way

to control the constraint violation by inducing a damped wave equation for the scalar field Ψ. The other Maxwell equation, in the ideal MHD limit, only gives the definition for the current density, since the electric field is given in terms of the velocity of the fluid and the magnetic field, that is,

$$E_i = -\epsilon_{ijk} v^k B^k. \tag{18}$$

Conservation of the stress-energy tensor in Eq. (13),

$$\nabla_a T^{ab} = 0, \tag{19}$$

provides four evolution equations for the fluid variables, namely, the velocity and the internal energy. Conservation of the baryon number

$$\nabla_a(\rho_o u^a) = 0 \tag{20}$$

leads to the evolution equation of the rest mass density ρ_o. Closure of the equations is achieved by introducing an equation of state (EOS) relating the pressure with the other thermodynamical quantities of the fluid, $P = P(\rho_o, \epsilon)$.

High resolution shock capturing schemes (HRSC) are robust numerical methods for compressible fluid dynamics. These methods, based on Godunov's seminal work [37], are fundamentally based on expressing the fluid equations as integral conservation laws. To this end, we introduce *conservative* variables $q = (D, S_i, \tau, B^i)^{\mathrm{T}}$, where

$$D = W\rho_o, \tag{21}$$

$$S_i = (h_e W^2 + B^2)v_i - (B^j v_j)B_i, \tag{22}$$

$$\tau = h_e W^2 + B^2 - P - \frac{1}{2}\left[(B^i v_i)^2 + \frac{B^2}{W^2}\right] - D, \tag{23}$$

and B^i is both a primitive and a conservative variable. In an asymptotically flat spacetime these quantities are conserved and are related to the total energy, momentum, and, in the nonrelativistic limit, the kinetic energy, respectively. The quantities $w = (\rho_o, v^i, P, B^i)^{\mathrm{T}}$ are called the *primitive* variables in contrast to the conservative variables. The fluid state can be specified using either set of variables, and both sets are required to write the MHD evolution equations. Anticipating the form of these equations, we also introduce the densitized conserved variables

$$\begin{aligned} \tilde{D} &= \sqrt{h}D, & \tilde{S}_i &= \sqrt{h}S_i, \\ \tilde{\tau} &= \sqrt{h}\tau, & \tilde{B}^i &= \sqrt{h}B^i, \end{aligned} \tag{24}$$

where $h = \det(h_{ij})$. The fluid equations can now be written in balance law form

$$\partial_t \tilde{q} + \partial_k f^k(\tilde{q}) = s(\tilde{q}), \tag{25}$$

where f^k are flux functions, and s are source terms. The fluid equations in this form are

$$\partial_t \tilde{D} + \partial_i\left[\alpha\tilde{D}\left(v^i - \frac{\beta^i}{\alpha}\right)\right] = 0, \tag{26}$$

$$\begin{aligned} \partial_t \tilde{S}_j &+ \partial_i\left[\alpha\left(\tilde{S}_j\left(v^i - \frac{\beta^i}{\alpha}\right) + \sqrt{h}Ph^i{}_j\right)\right] \\ &= \alpha^3\Gamma^i{}_{jk}(\tilde{S}_i v^k + \sqrt{h}Ph_i{}^k) + \tilde{S}_a\partial_j\beta^a - \partial_j\alpha(\tilde{\tau} + \tilde{D}) \\ &\quad - \zeta\alpha(\tilde{B}_i W^{-2} + v_i v_j \tilde{B}^j)\partial_k\tilde{B}^k, \end{aligned} \tag{27}$$

$$\begin{aligned} \partial_t \tilde{\tau} &+ \partial_i\left[\alpha\left(\tilde{S}^i - \frac{\beta^i}{\alpha}\tilde{\tau} - v^i\tilde{D}\right)\right] \\ &= \alpha\left[K_{ij}\tilde{S}^i v^j + \sqrt{h}KP - \frac{1}{\alpha}\tilde{S}^a\partial_a\alpha\right], \\ &\quad - \zeta\alpha v_j\tilde{B}^j\partial_k\tilde{B}^k, \end{aligned} \tag{28}$$

$$\begin{aligned} \partial_t \tilde{B}^b &+ \partial_i\left[\tilde{B}^b\left(v^i - \frac{\beta^i}{\alpha}\right) - \tilde{B}^i\left(v^b - \frac{\beta^b}{\alpha}\right)\right] \\ &= -\alpha\sqrt{h}h^{bi}\partial_i\Psi - \zeta\alpha v^i\partial_j\tilde{B}^j, \end{aligned} \tag{29}$$

$$\partial_t\Psi = -c_r\alpha\Psi - c_h\frac{\alpha}{\sqrt{h}}\partial_i\tilde{B}^i + (\beta^i - \alpha v^i)\partial_i\Psi, \tag{30}$$

where $c_r = \kappa$ and we have allowed for different speeds than light by introducing the parameter c_h. Except in the tests, we will use the original prescription (17) with $c_h = 1$. Here ${}^3\Gamma^i{}_{jk}$ is the Christoffel symbol associated with the 3-metric h_{ij}, and K is the trace of the extrinsic curvature, $K = K^i{}_i$. Notice that the aforementioned system is an extended version of the one employed in our earlier works [5,27,28]. Here we have added additional terms toggled by the parameter ζ, which allow for considering an extension of the "eight-wave" formulation which, in the absence of the cleaning field Ψ, ensures the strong hyperbolicity of the system [36] —at the cost of introducing derivative terms in the sources. Furthermore, by setting $\zeta = 1$, the propagation speeds of two constraint violating modes become nonvanishing, and hence violations are dragged along by the fluid's velocity. This is numerically convenient as possible violations will propagate off the grid.

Finally, we close the system of fluid equations with an EOS. We choose the ideal fluid EOS

$$P = (\Gamma - 1)\rho_o\epsilon, \tag{31}$$

where Γ is the constant adiabatic exponent. Nuclear matter in neutron stars is relatively stiff, and we set $\Gamma = 2$ in this work. When the fluid flow is adiabatic, this EOS reduces to the well-known polytropic EOS

$$P = \kappa\rho_o{}^\Gamma, \tag{32}$$

where κ is a dimensional constant. We use the polytropic EOS only for setting initial data.

The set of fluid equations, Eqs. (26)–(29), are used to evolve the conservative variables. However, these equa-

tions also contain the primitive variables, which necessitates a step in the evolution scheme that solves for the primitive variables in terms of the conservative ones. Given the primitive variables, the conservative variables are easily calculated from the algebraic expressions in Eqs. (24). Calculating the primitive variables from the conservative variables, however, is more delicate, as it requires the solution of a transcendental equation. To this end we first define the quantity $x \equiv h_e W^2$. We then write $S^2 = S^i S_i$ in terms of x and solve for W^2, obtaining

$$W^2 = \frac{x^2(x + B^2)^2}{x^2(x + B^2)^2 - x^2 S^2 - (2x + B^2)(S_i B^i)^2}. \quad (33)$$

Using the definition of τ, we define a function that is identically zero

$$f(x) = x - P - \frac{1}{2}\left[\frac{(S_i B^i)^2}{x^2} + \frac{B^2}{W^2}\right] + B^2 - \tau - D = 0. \quad (34)$$

If the enthalpy can be expressed as a simple function of the pressure, as can be done for the ideal fluid and a generalized EOS with a cold nuclear component, then we can express the pressure as a function x. For the ideal fluid EOS used here, the enthalpy equation

$$h_e = \frac{x}{W^2} = \rho_0 + \rho_0 \epsilon + P \quad (35)$$

can be solved for P by substituting in $\rho_0 = D/W$ and the EOS to obtain

$$P = \frac{\Gamma - 1}{\Gamma}\left(\frac{x}{W^2} - \frac{D}{W}\right). \quad (36)$$

Combining these equations, f is a function of a single unknown x. This equation can be solved numerically using the Newton-Raphson method. It is useful to note that x has a minimum physical value, which is found by requiring in Eq. (33) that $W^2 \geq 1$.

III. IMPLEMENTATION DETAILS

The code is constructed within the HAD computational infrastructure, which provides distributed adaptive mesh refinement (AMR). The AMR follows in the style of Berger and Oliger [38], but uses the tapering condition for AMR boundaries instead of temporal interpolation [39]. The combined set of geometric equations and fluid equations, Eqs. (5)–(7) and (26)–(30), respectively, is discretized using the method of lines. The geometric equations are discretized using operators that satisfy a summation by parts property [40,41]. The fluid equations are discretized using the Harten–Lax–van Leer–Einfeldt (HLLE) method [42]. The semidiscrete equations are solved using a third order accurate, total variation diminishing Runge-Kutta solver [43].

The fluid equations diverge as the density goes to zero, and, as is standard practice, we disallow any true vacuum by setting such regions to a floor or atmosphere value. The floor is applied after each fluid update as

$$D \leftarrow \min(D, \delta), \qquad \tau \leftarrow \min(\tau, \delta), \quad (37)$$

where δ is chosen to be many orders of magnitude smaller than the maximum densities and pressures in the initial data. The comparison of otherwise identical runs but with different floor values suggests that the use of an atmosphere generally does not affect accuracy.

We have, however, found certain issues with precision occurring within the primitive solver. Typical maximum values of the density are about 10^{-2} in geometric units, with a floor value of $\delta = 10^{-8}$. We have found it useful therefore to scale Newton's constant G such that the fluid densities and pressures are close to order unity. Thus, rather than using the typical choice of $G = 1$, we might use $G = 1/1000$. As G affects only the coupling of the fluid to the geometry, the evolution of the geometric equations is not affected by this scaling. Empirically, we find that scaling G allows the primitive variables to be more easily recovered in low density regions. This improvement appears to be related to finite precision effects in the primitive solver. The scaling decreases the effective floor value while avoiding the problems associated with having a true vacuum.

The Maxwell equations require that the magnetic field be divergenceless. This is the so-called "no monopole" constraint. A variety of schemes exist with the goal of controlling the growth of the divergence. We choose a strategy that ensures flexibility and robustness when dealing with multiple grid structure (as in AMR) and allows, in principle, for a clean boundary treatment [44]. To this end we have implemented hyperbolic divergence cleaning as described in [36] (also see [45]). We thus introduce a scalar $\Psi(x, y, z, t)$ that is sourced by the negative of the divergence of the magnetic field as shown in Eq. (30). As described in [36], this scheme implies that the divergence obeys a damped wave equation so that constraint violations propagate off the grid and their value is reduced.

For initial data generated with Magstar, the divergence is around machine precision, and so to test the implementation of divergence cleaning, we introduce a perturbation to the magnetic field in order to produce a significant amount of divergence to the magnetic field. In particular, this perturbation takes the form of a spherical, Gaussian shell of radius r_o, width δ, and amplitude A added to each component of $\vec{B}$. We expect the divergence cleaning to propagate this perturbation as a damped wave, and we therefore plot the scaled quantity $x^2[\vec{\nabla} \cdot \vec{B}]$ in Fig. 1. As can be seen by comparing the cases of no cleaning (top) and with cleaning (bottom), the divergence propagates with damping through the refinement boundaries across the grid.
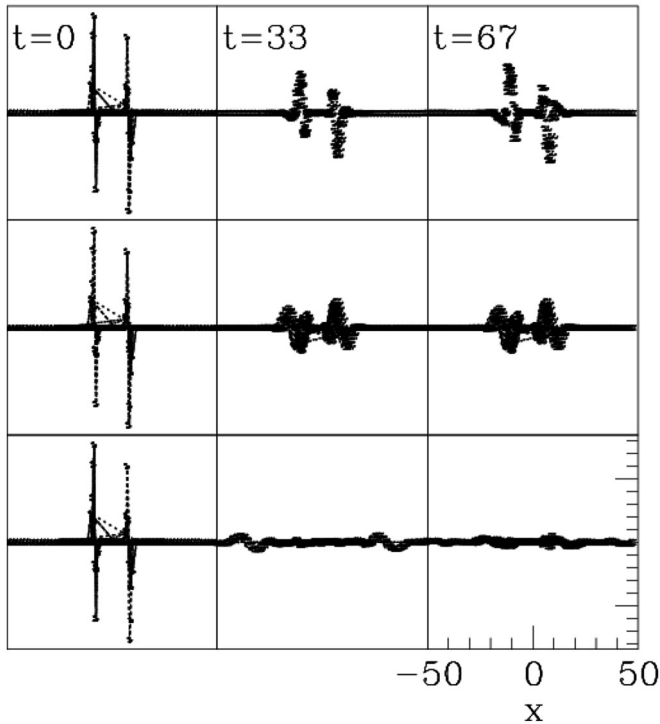
FIG. 1. Demonstration of the effectiveness of divergence cleaning at handling deviations from a divergenceless magnetic field. A calculation of the divergence of the magnetic field, $x^2[\vec{\nabla} \cdot \vec{B}]$, along the x axis for 3 times is shown for each of three cases: (top) No divergence cleaning; (middle) Cleaning with $c_h = 0.1$ and $c_r = 0.01$; and (bottom) Cleaning with $c_h = 1.0$ and $c_r = 0.1$. These runs were otherwise identical for a magnetized, rotating star of coordinate equatorial radius of 10 with spin along the z axis with three levels of refinement (at ± 50, ± 25, and ± 12.5) and a perturbation to the magnetic field to introduce an explicit deviation from divergenceless. Concentrating on the MHD equations, the metric terms were frozen at their initial values, e.g. the Cowling approximation. The bottom row shows clear wavelike behavior as it "cleans" the divergence.

As typical with codes dealing with linearly degenerate hyperbolic systems, like those employed in numerical relativity, a dissipation operator is applied to the metric variables. This operation uses a high-order derivative to serve as a low-pass filter and does not affect the accuracy of the simulation. We have found it useful for keeping things smooth. Although this operation is not applied to the fluid variables, we have found it quite important in keeping the magnetic field components smooth. The magnetic field evolution is coupled tightly with that of the velocity, and any nonsmoothness that appears in the velocity can easily affect the smoothness of the magnetic field. The addition of dissipation to the magnetic field and divergence cleaning field helps control the behavior of the magnetic field.

At the boundaries of the domain, simple outflow boundary conditions are applied to the fluid variables. This is accomplished by copying the values of the conservative variables near the boundary outward. Most of the gravita-

tional variables are treated using Sommerfeld-like boundary conditions of the form [46]

$$\left(\partial_t + \partial_r + \frac{1}{r}\right)(g_{ab} - \eta_{ab}) = 0, \tag{38}$$

where η_{ab} is just the Minkowski metric. The rest, which are not so crucial, are set by either maximally dissipative [2] or constraint preserving boundary conditions [31].

A relevant issue when considering the collapse of stars is the formation of a black hole. To deal with such situations, we adopt black hole excision where we dynamically monitor for the appearance of trapped surfaces (which lie inside an event horizon if cosmic censorship holds) and excise cubical region(s) from the computational domain. As discussed in [47,48], this excision introduces inner boundaries that are of "outflow" type, and so no boundary condition is required there. However, for a more robust handling of the fluid, we also allow for a modification of the fluid equations inside the trapped surface [7]. The MHD equations are written in balance law form

$$\dot{U} + F(U)' = S, \tag{39}$$

which we modify to include a damping term near the black hole

$$\dot{U} + F(U)' = S - f(r)(\Delta x)^p (U - U_0). \tag{40}$$

Here the function $f(r)$ decreases smoothly with r, from a given value at the excision region to zero at the outermost trapped surface (OTS) found, and is zero for $r \geq r_{\text{OTS}}$, so that the exterior of the black hole is causally disconnected from the effect of this extra term. U_0 is set to zero or to the value of the atmosphere if the corresponding field has one. The coefficient $(\Delta x)^p$ ensures that the damping term converges to zero as the grid spacing Δx is reduced. As long as one chooses p greater than or equal to the order of convergence of the code, this term will not modify the convergence rate. We typically adopt a value of $p = 4$.

Finally, gravitational radiation is calculated via the evaluation of the Newman-Penrose scalar Ψ_4, which is computed by contracting the Weyl tensor, C_{abcd}, with a suitably defined null tetrad $\{\ell, n, m, \bar{m}\}$,

$$\Psi_4 = C_{abcd} n^a \bar{m}^b n^c \bar{m}^d, \tag{41}$$

extracted at spherical surfaces Σ_i located in the wave zone, far from the sources. We also consider possible corrections required to deal with gauge ambiguities, as discussed in [49]. We refer the reader to that paper for details on the adopted tetrad and required corrections.

IV. DIAGNOSTIC QUANTITIES

The initial configuration for the stars is axisymmetric, and we therefore want to be able to measure any change to this structure. For this purpose, we monitor certain distortion parameters [50] defined as

$$\eta_+ = \frac{I^{xx} - I^{yy}}{I^{xx} + I^{yy}}, \tag{42}$$

$$\eta_\times = \frac{2I^{xy}}{I^{xx} + I^{yy}}, \tag{43}$$

$$\eta = \sqrt{\eta_+^2 + \eta_\times^2}, \tag{44}$$

in terms of the moment of inertia tensor

$$I^{jk} \equiv \int D x^j x^k d^3 x. \tag{45}$$

These parameters are computed with respect to the conservative variable D.

It is also standard practice to display the maximum of the (primitive) rest mass density, and we compute the fractional change in time as

$$\Delta\rho \equiv \frac{\max|\rho_0(t)| - \max|\rho_0(0)|}{\max|\rho_0(0)|}. \tag{46}$$

Generally, for stable stars one sees this quantity oscillate from inherent numerical perturbations about a stable solution. For unstable solutions, one expects this quantity to change in a significant way. Similarly, we compute the relative change in baryon mass as a function of time as

$$\Delta M_{\text{baryon}} \equiv \frac{M_{\text{baryon}}(t) - M_{\text{baryon}}(0)}{M_{\text{baryon}}(0)}, \tag{47}$$

where

$$M_{\text{baryon}} \equiv \int D dV. \tag{48}$$

This mass is related to the expected baryon number and should be strictly conserved as long as mass is not leaving the computational domain. Many HRSC schemes explicitly conserve this quantity, but here it is not *a priori* conserved. Our use of an atmosphere entails adding a small amount of mass in regions that would otherwise become evacuated. Another reason is that we are using a finite difference based AMR, which does not accommodate as readily a strictly conservative treatment as a finite volume method would [51]. Finally, the presence of source terms in the evolution equations for the other conservative variables also breaks perfect conservation of these other quantities.

We also compute the angular momentum of the fluid. Since our stars rotate about the z axis, we need only compute a single such quantity

$$J_z = \int (x n^j T_{jy} - y n^j T_{jx}) \sqrt{h} d^3 x. \tag{49}$$

The use of Cartesian coordinates is typically avoided when one expects angular momentum to be conserved since cylindrical coordinates are better adapted to the respective Killing vector. However, because this project is part of a more general effort to model a variety of systems with different natural coordinates and no symmetries, we simply monitor the extent to which this is conserved by computing a fractional change as

$$\Delta J_z \equiv \frac{J_z(t) - J_z(0)}{J_z(0)}. \tag{50}$$

Finally, we also monitor the extent to which our numerical solution satisfies the Einstein equations as expressed in Eq. (1). That is, we compute the so-called residual of these equations, expressed as the four-vector Z^a as in Eq. (9). In particular, we monitor the norm of this vector

$$|\vec{Z}| \equiv \|Z^a\|_2. \tag{51}$$

Analytical solutions to Einstein equations must have a vanishing residual, and thus we monitor this residual for solutions obtained at various resolutions to check for convergence to a consistent solution.

V. INITIAL DATA

We use initial data generated with the program `Magstar`, part of the LORENE software package. These solutions are described in [19] and are rigidly rotating, magnetized neutron stars. They are generated as fully consistent solutions of Einstein's equations as opposed to taking nonmagnetized stars and adding a seed magnetic field without re-solving the constraints. The initial magnetic field is dipolar and aligned with the rotation axis, produced by a current function $f(A_\phi) = \text{const}$, where A_ϕ is the toroidal component of the electromagnetic potential vector.

To get a handle on the solutions generated, we first turn off the magnetic field and compute the "usual" two-parameter solution space as described in [52]. Using the terminology of [19], we compute solutions based on the two parameters of central enthalpy and frequency. Examination of Eq. (13) of [19] shows that the log-central enthalpy H_c is related to the entropy used here [h_e as defined in Eq. (14)] by

$$H_c = \ln(h_e) + C, \tag{52}$$

where C is constructed by physical constants and h_e is evaluated at the center of the star.

These nonmagnetized solutions are diagrammed in a plot of total gravitational mass versus central enthalpy in Fig. 2. The lower curve shows the static limit for stars that are not rotating. The upper curve is the mass shedding limit, represented by the largest frequency for which `Magstar` returned a solution. These curves serve as the upper and lower bounds on the solution space of stationary, unmagnetized stars. It should be noted that `Magstar` generates only rigidly rotating stars, and therefore the evolutions are far from the fast rotating regime expected to excite large and growing nonaxisymmetric modes.

We also compute and show a sequence of stars at constant baryon mass. Such sequences are important because real stars are expected to conserve baryon mass as they evolve, and thus the sequences are expected to approximate their evolution. Furthermore, along such sequences it has
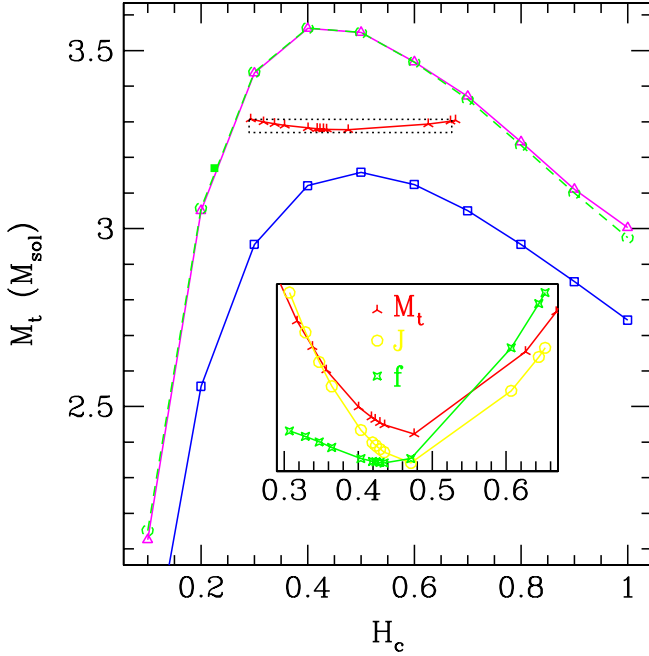
FIG. 2 (color online). Diagram of solution space of stars generated with `Magstar` (using its units). The total gravitational mass is plotted versus the central enthalpy. The upper curve (purple, open triangles) represents stars with no magnetic field at the mass shredding limit. Very close to this are shown (green, open circles) stars rotating at the same frequencies but with a radial magnetic field at the pole of $1000 \, GT = 10^{16}$ G. The masses of these stars are barely changed with respect to their nonmagnetic counterparts. The lower curve (blue, open squares) represents the static limit with no rotation. A sequence of constant baryon mass stars ($M_B = 3.6 M_{sol}$) is shown (red stars). This sequence is also shown in the inset along with their angular momentum (yellow, open circles) and frequency of rotation (green stars). The location of the initial data used in the initial data convergence test of Fig. 3 and the long term, stability test of Fig. 4 is also shown (green, solid square) although that solution strictly does not belong here because it has a nonvanishing magnetic field.

been shown that there is a stability change at the minimum in the angular momentum [52]. Looking at the inset of Fig. 2, one therefore expects the solutions on the right to be unstable while those on the left should remain stable.

Note that the addition of a nonvanishing magnetic field adds another dimension to this diagram although the effect of the magnetic field on the initial data is not so dramatic. Certainly there are many ways in which to "add" a magnetic field to a stellar solution. In [19] a nonvanishing current is assumed and a solution is obtained with the same baryon mass but now with nonvanishing magnetic field. In particular, solutions at the mass shedding limit with no magnetic field are shown in Fig. 2 by open triangles. Almost indistinguishable from these solutions are those magnetized such that the radial magnetic field at the pole of the star is 1000 gigatesla (GT) or 10^{16} G, shown with open circles.

We consider different perturbations. To perturb the pressure, we decrease it according to real parameters A_p and m in terms of the unperturbed pressure p_0 depending on the azimuthal angle φ

$$p = p_0[1 - A_p \sin^2(m\varphi)]. \tag{53}$$

We also consider perturbations to the rest mass density decreasing it everywhere by a fraction A_ρ

$$\rho = \rho_0[1 - A_\rho]. \tag{54}$$

We verify the initial data in our evolution code in a number of ways. We examine convergence of the data to a unique solution which solves the constraints. In Fig. 3 we show the residual of the Hamiltonian and y component of the momentum constraint for three different resolutions. The Hamiltonian constraint is a good measure of the fidelity of the solution to the Einstein equations, and, as is clear from the figure, its residual decreases rapidly with
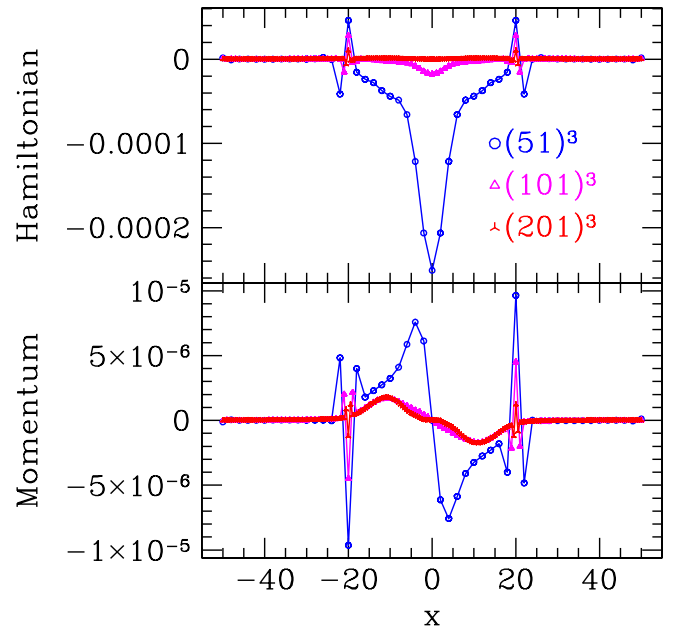

FIG. 3 (color online). The residuals of two constraint equations, namely, the Hamiltonian constraint and the y component of the momentum constraint. A slice along the x axis of the computed residuals for various unigrid resolutions. Top: That the Hamiltonian constraint residual converges to zero with increasing resolution is taken as evidence that the initial data are properly constructed and read into the code. Bottom: That the momentum constraint residual improves with the first increase in resolution is similar evidence. However, the next increase in resolution fails to bring down this residual. We suspect that this remaining error is associated not with truncation error but instead with inherent errors in the numerical transformation and interpolation from LORENE's spherical basis to our Cartesian one. Note the spikes that arise at the stellar boundaries due to discontinuities in the fluid variables;, these are not expected to converge to zero.

resolution. Furthermore, we confirm that the divergence of the magnetic field is around machine precision.

VI. RESULTS

A. Stable, rotating star test

Before addressing the effects of the magnetic field, we verify that the code reproduces the expected behavior as described, for example, in [53]. First, we consider evolutions of stable, rotating stars and find that the code evolves
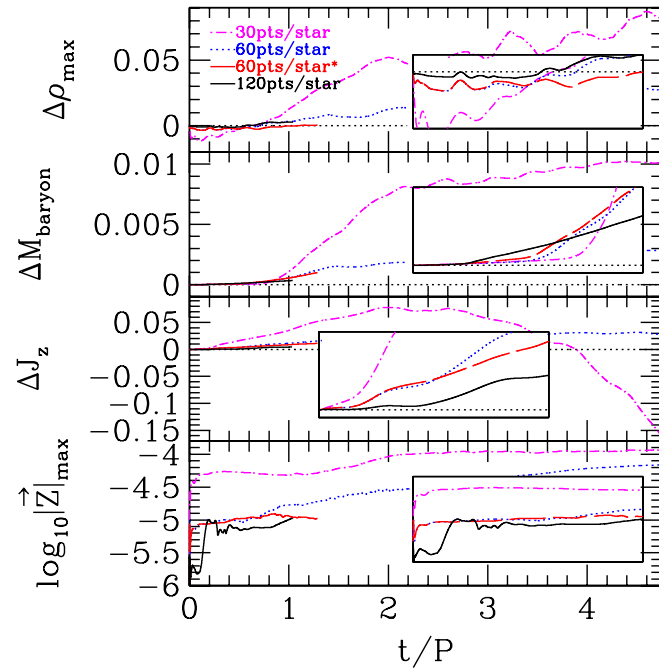

FIG. 4 (color online).   Convergence results for the evolution of a stable, nonmagnetized, rotating star (the particular initial solution is shown in Fig. 2 as a green solid square). Three fixed mesh refinement evolutions are shown, each with a multiple of the coarsest resolution resolving the equator of the star with the following: (magenta, dot-dashed line) 30 points/star, (blue, dotted line) 60 points/star, and (black, solid line) 120 points/star. Also shown is a run with the same stellar resolution of (red, long-dashed line) 60 points/star but with a coarse grid that extends twice as far in all directions. The two highest resolution runs were terminated early because of the computational cost, not because of any robustness problems. The insets show the same data but in finer detail for the first rotational period. The top frame shows the fractional change in maximum density versus rotational period. With increasing resolution the solution better approximates a stationary solution. The upper middle frame shows the fractional change in the baryon mass, Although our scheme, using vertex centered AMR, an atmosphere, and full general relativity with sources, is not strictly conservative, the plot shows that deviations from strict conservation are small and decrease with more resolution. The lower middle frame shows the fractional change in integrated angular momentum. Again, the code demonstrates convergence to conservation. The bottom frame shows the maximum of the norm of the Z^a constraint residuals as a function of time that also converge.

such a star as long as desired while maintaining a stationary solution. This is a demanding test as it depends on the balance between gravitational and hydrostatic forces in a rotating configuration with both a nonconforming grid and variables not adapted to the symmetries of the problem.

One example of the behavior of the numerical solution is shown in Fig. 4. As apparent in the top frame of the figure, the fractional change in the maximum of the density oscillates with a slow overall increase. This oscillation is characteristic of quasinormal ringing of the star excited by inherent numerical error. However, the figure shows data for a number of resolutions, and the trend as resolution improves is toward a flatter curve. This trend is particularly apparent in the inset, which shows just the first rotational period. This behavior suggests that the code is converging to the continuum solution.

In addition to the runs with varying resolution, Fig. 4 shows another evolution with a coarse level extending twice as far but with fine levels identical to the medium resolution run just discussed. Generally, the results are the same as for the nonextended domain, indicating little effect from the boundary for the first half-period.

Although the fluid scheme used here is not strictly conservative because of (i) AMR boundaries for our vertex centered scheme, (ii) our outer boundary treatment, and (iii) our use of a fluid floor, Fig. 4 shows that the fractional change in the volume-integrated baryon mass remains constant to a high degree. Similarly, the integrated angular momentum of the fluid converges to conservation.

Finally, the bottom frame of Fig. 4 shows the maximum value of the constraint violation. These values increase with time as the numerical error accumulates, but higher resolution runs demonstrate less violation though it saturates due to the intrinsic error of the initial and boundary data.

B. Unstable, rotating, magnetized star test

Similarly, we evolve a rotating, magnetized star located on the unstable side. These stars, perturbed by inherent numerical error, collapse to black holes. We see no evidence of significant disk formation (as in e.g. [15,16,54–56]). Notice that even though we do not impose any type of symmetry, no asymmetric, unstable modes are observed. This behavior is consistent with previous work that studied the possible onset of axisymmetric instabilities [57]. These previous studies found that such instabilities require high rotation rates characterized by $T/W > 0.25$ in contrast to those studied here for which $T/W \leq 0.1$. Consequently, we see no evidence for deformations of the star as would be apparent by monitoring the distortion parameters moving away from zero.

In Fig. 5, we show an example of such an evolution at three successively finer resolutions. Because the star is collapsing, the maximum density increases dramatically.
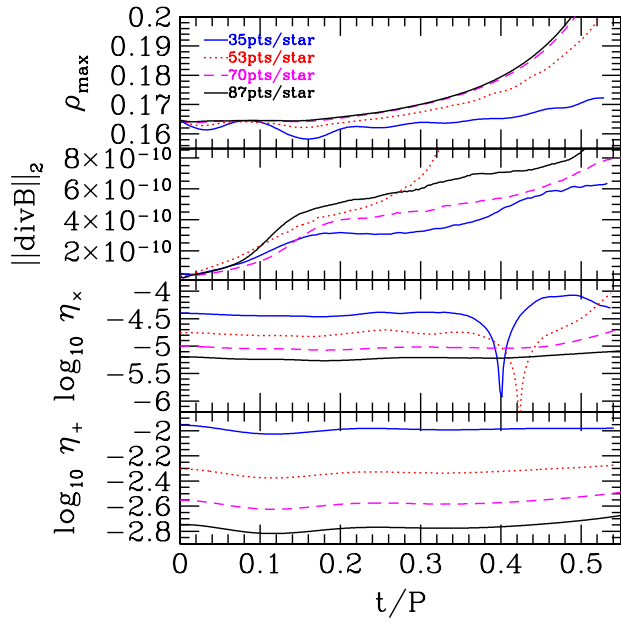
FIG. 5 (color online). Collapse to black hole of an unstable, unperturbed, magnetized star for multiple of a base resolution. The initial datum is an unperturbed `Magstar` solution with central enthalpy $H_c = 0.8$ rotating at a frequency $f = 835$ Hz and with polar magnetic field of 1000 GT $= 10^{16}$ G. The top frame shows the maximum density, which increases with time as the star collapses. The upper middle frame shows a norm of the divergence of the magnetic field. The lower frames show the distortion parameters of the D field as functions of time.
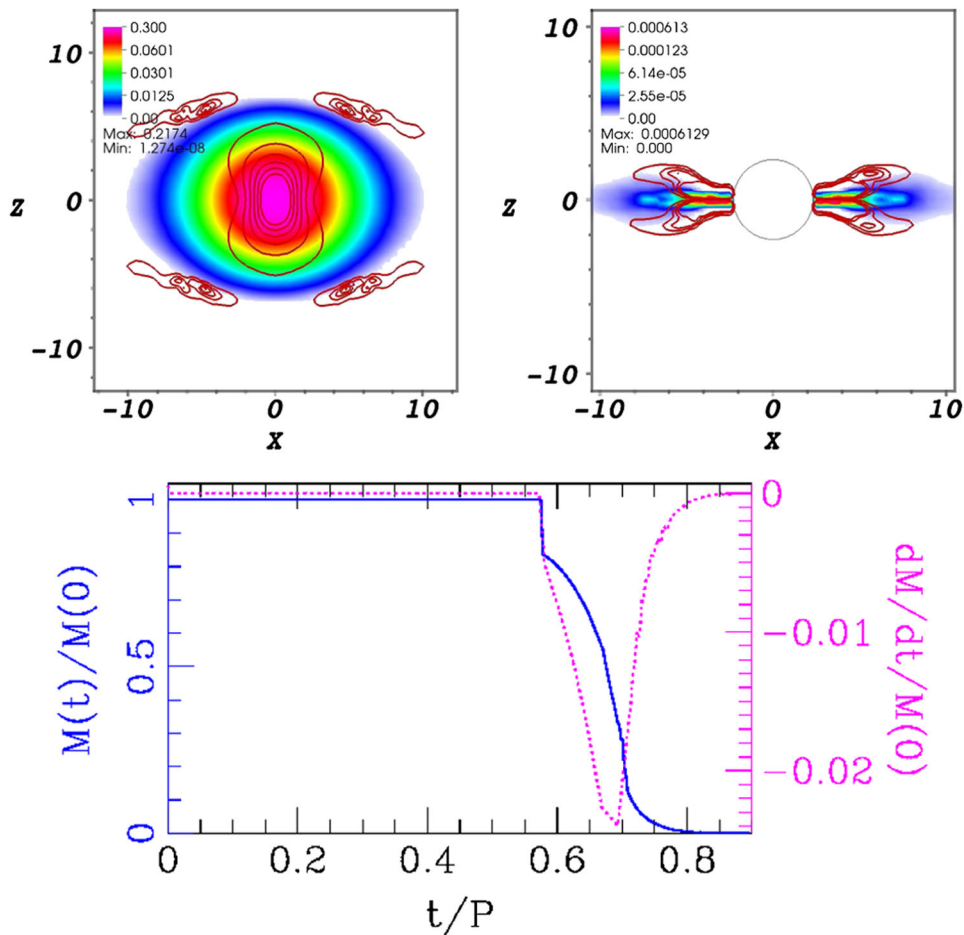
FIG. 6 (color online). Density ρ_0 and magnetic field strength on the $y = 0$ plane for the same star as shown in Fig. 5. The density is shown with respect to the color map while the contours denote the magnetic field, which is equally spaced from 0 to 5×10^{15} G. The top left corresponds to $t = 0.5P$ while the top right to $t = 0.9P$ (the circle shown represents the apparent horizon.) The bottom plot illustrates the normalized mass as a function of time, along with its rate of change.

The magnetic field remains essentially poloidal throughout the collapse and its maximum magnitude increases due to the resulting compression of the field lines. Despite this increase, the magnetic field plays no important role in the collapse since its associated pressure is still several orders of magnitude smaller than the fluid pressure. While we do observe an increase in the norm of the divergence, the growth is not particularly fast and the divergence remains small in absolute terms and relative to the magnetic field.

Figure 6 displays two snapshots of the density and magnetic field strength of the collapsing star tested in Fig. 5. The first one illustrates a stage during the collapse before an apparent horizon forms. The second one shows the behavior after an apparent horizon is found and its interior excised. The apparent horizon appears at $t \simeq 0.6P$, when the maximum of the density is $\rho_{max} = 0.271$ and the minimum of the lapse is $\alpha_{min} = 0.2$.

C. Perturbations of unstable stars

Previous work presented in [53] argues that, in general, unstable stars should either collapse to a black hole or expand and oscillate about a stable stellar solution. Seeking to duplicate this behavior, we perturb an unstable star. Indeed, as shown in Fig. 7, we find precisely the behavior described. If our perturbation increases the pressure sufficiently, we find a star that expands and oscillates about some other, presumably stable solution. However, if we choose a perturbation that barely increases the pressure, the star collapses to a black hole.

However, given the interest in black hole critical phenomena (see [58,59]) over the past couple of decades, we study in detail the separation between these two behaviors.
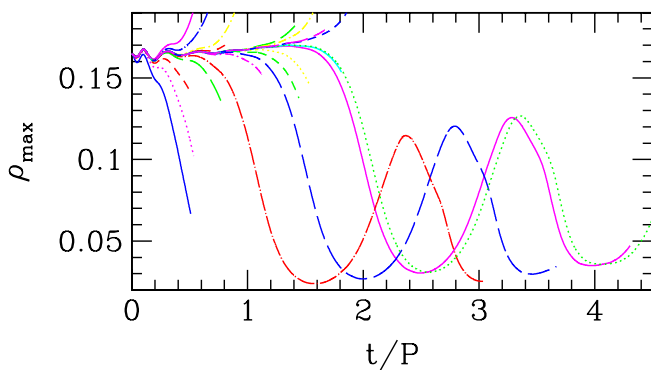

FIG. 7 (color online).   The maximum density ρ_{max} as a function of time for an unstable, perturbed [$m = 3$ in Eq. (53)], nonmagnetic, rotating star. The (unperturbed) initial star has central enthalpy 0.8 and rotates at the mass shedding limit. Solutions resulting from tuning the amplitude of the perturbation A_p to roughly one part in 10^6 show the two disparate outcomes (as discussed in [53]): collapse to black hole or violent oscillations about a stable stellar solution with equivalent mass. With more tuning, the star resembles the initial, unstable solution for a longer time.

That is, we continue to adjust A_p in Eq. (53) searching for a value A_p^* above which one finds black hole formation and below which one finds an expanding solution (the way we have parametrized the pressure perturbation, $A_p^* < 0$).

As apparent from Fig. 7, the more one continues this tuning, the longer the unstable star survives. This type of tuning is reminiscent of a similar analysis of an unstable, irregular static solution [60]. What these results suggest is that the unstable solution (i) sits at the threshold of black hole formation with (ii) a single unstable mode. That small perturbations about the solution send it either to collapse or expansion suggests that it sits at the threshold. Furthermore that a single parameter is sufficient to stabilize the solution suggests that there is a single unstable mode. In contrast, sometimes one can tune multiple parameters to find a threshold solution [61].

If these suggestions hold up, these would suggest that at least some of these unstable solutions might serve as type I critical solutions. Indeed, previous work [62] perturbed stable TOV stars in spherical symmetry and found unstable TOV stars at criticality in type I collapse. In that work, they were able to achieve phenomenal resolution and tuning. In contrast, while they perturbed a self-consistent *stable* solution and saw the tuned evolution driven to the *unstable* branch of solutions, here we begin with the unstable solution and perturb around it. Here, we have only been able to tune to about one part in a million, being prevented from tuning further because successive evolutions stop the trend toward longer lived solutions. That such searches are prevented from continuing might indicate some new phenomena, or, more likely, that boundary effects and numerical error begin to spoil the threshold behavior.

We have looked for a scaling law in the survival times of these tuned unstable stars. To the extent that this rough tuning is representative of the overall behavior, we find that the different solutions appear to scale as expected. However, because our searches have terminated so far from criticality, we cannot have much confidence in a precise scaling relationship. There has been recent work in the axisymmetric collision of neutron stars [63,64] that appears to demonstrate the same type of critical behavior as observed in [62].

We find the same type of behavior about a magnetized star as shown in Fig. 8. Here we have carried out three searches by varying a different parameter all perturbing the same solution. The figure makes apparent the same ringing for all three families, although the amplitude varies across the different tuning families. It seems reasonable to take the results of these tunings as further evidence that only a single mode is unstable since if there were more unstable modes, these different tunings would produce solutions more varied from each other. We have begun to look at the geometry of the purported unstable mode by looking at the difference $\Delta = \rho_0(t) - \rho_0(0)$ at late times for near-critical evolutions. These calculations indicate the mode is
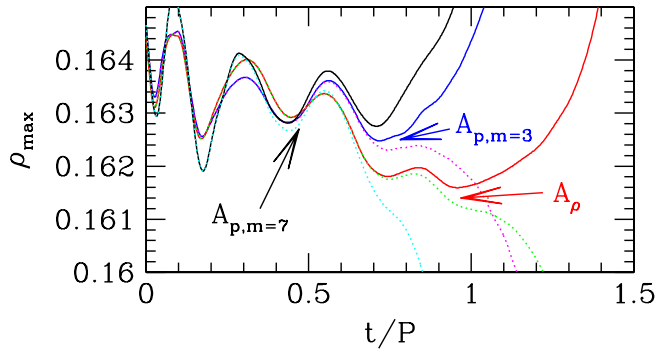
FIG. 8 (color online). Results of three critical searches for a magnetized, rotating star with central enthalpy of 0.8 and a radial magnetic field at the pole of 1000 GT. One search varied the amplitude of the pressure perturbation A_p with $m = 7$ (black and cyan lines), another with $m = 3$ (blue and magenta lines), and another varied the density perturbation A_ρ. In solid lines are shown the supercritical evolutions that collapse to black holes, while subcritical solutions for the two searches are shown with dotted lines. The search over pressure with $m = 7$ achieved tuning to about one part in 10^3, that with $m = 3$, one part in 10^4, and that over density achieved about one part in 10^5.

likely axisymmetric with differences between Δ on the $x = 0$ plane and Δ on the $y = 0$ plane being at about the 10% level.

VII. CONCLUSIONS

We study the evolution of rotating stellar configurations and examine different phenomenology related to stability and magnetic field influence in their dynamical behavior. The stars are constructed assuming a polytropic equation of state using the code Magstar, which is part of the publicly available LORENE package. We present several studies that indicate our code reliably and robustly evolves astrophysically relevant scenarios including magnetic field effects. We study the dynamical effect of perturbations of stars on the unstable branch of solutions. We find evidence that these unstable solutions may play a similar role as the unstable TOV stars play in spherically symmetric evolu-

tions as studied in [62]. This is significant because it suggests that the addition of angular momentum, magnetic field, and three dimensions do not allow for a multitude of unstable modes. Needless to say, the phenomena associated with the threshold of gravitational collapse merit further study.

Beyond the studies considered in this work, further interesting phenomenology to consider include the impact of magnetic fields in the stability of the star, a thorough analysis of the possible critical phenomena observed, and differences due to more realistic equations of state. The investigation of such scenarios will be presented elsewhere.

[1] N. Stergioulas, Living Rev. Relativity **6**, 3 (2003), http://relativity.livingreviews.org/Articles/lrr-2003-3/.
[2] C. Palenzuela, I. Olabarrieta, L. Lehner, and S. Liebling, Phys. Rev. D **75**, 064005 (2007).
[3] C. Palenzuela, L. Lehner, and S. L. Liebling, Phys. Rev. D **77**, 044036 (2008).
[4] M. Anderson *et al.*, Phys. Rev. D **77**, 024006 (2008).
[5] M. Anderson *et al.*, Phys. Rev. Lett. **100**, 191101 (2008).
[6] C. Palenzuela, M. Anderson, L. Lehner, S. L. Liebling, and D. Neilsen, Phys. Rev. Lett. **103**, 081101 (2009).
[7] M. Megevand *et al.*, Phys. Rev. D **80**, 024012 (2009).
[8] M. Shibata and Y.-i. Sekiguchi, Phys. Rev. D **69**, 084024 (2004).
[9] M. D. Duez, Y. T. Liu, S. L. Shapiro, and M. Shibata, Phys. Rev. D **73**, 104015 (2006).
[10] K. Kiuchi, M. Shibata, and S. Yoshida, Phys. Rev. D **78**, 024029 (2008).
[11] *Petascale Computing: Algorithms and Applications*, edited by D. Bader (Chapman & Hall/CRC, London, 2007).

[12] B. Zink *et al.*, Phys. Rev. D **76**, 024019 (2007).
[13] M. Shibata, Astrophys. J. **595**, 992 (2003).
[14] M. D. Duez, S. L. Shapiro, and H.-J. Yo, Phys. Rev. D **69**, 104016 (2004).
[15] L. Baiotti *et al.*, Phys. Rev. D **71**, 024035 (2005).
[16] B. C. Stephens, S. L. Shapiro, and Y. T. Liu, Phys. Rev. D **77**, 044001 (2008).
[17] M. Shibata, M. D. Duez, Y. T. Liu, S. L. Shapiro, and B. C. Stephens, Phys. Rev. Lett. **96**, 031102 (2006).
[18] M. Shibata, Y. T. Liu, S. L. Shapiro, and B. C. Stephens, Phys. Rev. D **74**, 104026 (2006).
[19] M. Bocquet, S. Bonazzola, E. Gourgoulhon, and J. Novak, Astron. Astrophys. **301**, 757 (1995).
[20] B. Giacomazzo and L. Rezzolla, Classical Quantum Gravity **24**, S235 (2007).
[21] H. Sotani, K. D. Kokkotas, N. Stergioulas, and M. Vavoulidis, arXiv:astro-ph/0611666.
[22] H. Sotani, K. D. Kokkotas, and N. Stergioulas, Mon. Not. R. Astron. Soc. **375**, 261 (2007).
[23] S. Mereghetti, Astron. Astrophys. Rev. **15**, 225 (2008).
[24] A. M. Beloborodov and C. Thompson, Astrophys. J. **657**, 967 (2007).
[25] B. Haskell, L. Samuelsson, K. Glampedakis, and N. Andersson, Mon. Not. R. Astron. Soc. **385**, 531 (2008).
[26] N. Andersson and G. L. Comer, Living Rev. Relativity **10**, 1 (2005), http://relativity.livingreviews.org/open?pubNo= lrr-2007-1&page=articlesu6.html .
[27] D. Neilsen, E. W. Hirschmann, and R. S. Millward, Classical Quantum Gravity **23**, S505 (2006).
[28] M. Anderson, E. Hirschmann, S. L. Liebling, and D. Neilsen, Classical Quantum Gravity **23**, 6503 (2006).
[29] H. Friedrich, Commun. Math. Phys. **100**, 525 (1985).
[30] D. Garfinkle, Phys. Rev. D **65**, 044029 (2002).
[31] L. Lindblom, M. A. Scheel, L. E. Kidder, R. Owen, and O. Rinne, Classical Quantum Gravity **23**, S447 (2006).
[32] C. Bona, T. Ledvinka, C. Palenzuela, and M. Zacek, Phys. Rev. D **66**, 084013 (2002).
[33] C. Gundlach, J. Garcia, G. Calabrese, and I. Hinder, Classical Quantum Gravity **22**, 3767 (2005).
[34] J. M. Marti and E. Müller, Living Rev. Relativity **2**, 3 (1999), http://relativity.livingreviews.org/Articles/ lrr-2003-7/.
[35] J. A. Font, Living Rev. Relativity **3**, 2 (2000), http:// relativity.livingreviews.org/Articles/lrr-2003-4/cite.html.
[36] A. Dedner, F. Kemm, D. Kröner, C.-D. Munz, T. Schnitzer, and M. Wesenberg, J. Comput. Phys. **175**, 645 (2002).
[37] S. K. Godunov, Mat. Sb. **47**, 271 (1959).
[38] M. J. Berger and J. Oliger, J. Comput. Phys. **53**, 484 (1984).
[39] L. Lehner, S. L. Liebling, and O. Reula, Classical Quantum Gravity **23**, S421 (2006).
[40] B. Strand, J. Comput. Phys. **110**, 47 (1994).
[41] G. Calabrese, L. Lehner, D. Neilsen, J. Pullin, O. Reula, O. Sarbach, and M. Tiglio, Classical Quantum Gravity **20**, L245 (2003).
[42] A. Harten, P. D. Lax, and B. van Leer, SIAM Rev. **25**, 35 (1983).
[43] C.-W. Shu and S. Osher, J. Comput. Phys. **77**, 439 (1988).
[44] M. Cecere, L. Lehner, and O. Reula, Comput. Phys. Commun. **179**, 545 (2008).
[45] G. Tóth, J. Comput. Phys. **161**, 605 (2000).
[46] O. Rinne, L. Lindblom, and M. A. Scheel, Classical Quantum Gravity **24**, 4053 (2007).
[47] M. Tiglio, L. Lehner, and D. Neilsen, Phys. Rev. D **70**, 104018 (2004).
[48] G. Calabrese, L. Lehner, O. Reula, O. Sarbach, and M. Tiglio, Classical Quantum Gravity **21**, 5735 (2004).
[49] L. Lehner and O. M. Moreschi, Phys. Rev. D **76**, 124040 (2007).
[50] L. Baiotti, R. De Pietri, G. M. Manca, and L. Rezzolla, Phys. Rev. D **75**, 044023 (2007).
[51] M. Berger and P. Collella, J. Comput. Phys. **82**, 64 (1989).
[52] G. B. Cook, S. L. Shapiro, and S. A. Teukolsky, Astrophys. J. **424**, 823 (1994).
[53] J. A. Font, T. Goodale, S. Iyer, M. Miller, L. Rezzolla, E. Seidel, N. Stergioulas, W.-M. Suen, and M. Tobias, Phys. Rev. D **65**, 084024 (2002).
[54] T. W. Baumgarte and S. L. Shapiro, Astrophys. J. **585**, 930 (2003).
[55] I. Hawke, E. Schnetter, L. Baiotti, and L. Rezzolla, Comput. Phys. Commun. **169**, 374 (2005).
[56] M. D. Duez, Y. T. Liu, S. L. Shapiro, M. Shibata, and B. C. Stephens, Phys. Rev. Lett. **96**, 031101 (2006).
[57] G. M. Manca, L. Baiotti, R. De Pietri, and L. Rezzolla, Classical Quantum Gravity **24**, S171 (2007).
[58] M. W. Choptuik, Phys. Rev. Lett. **70**, 9 (1993).
[59] C. Gundlach and J. M. Martin-Garcia, Living Rev. Relativity **10**, 5 (2007), http://relativity.livingreviews.org/ Articles/lrr-2007-5/.
[60] M. W. Choptuik, E. W. Hirschmann, and S. L. Liebling, Phys. Rev. D **55**, 6014 (1997).
[61] S. L. Liebling, Phys. Rev. D **58**, 084015 (1998).
[62] S. Noble, Ph.D. thesis, The University of Texas at Austin, 2003.
[63] K.-J. Jin and W.-M. Suen, Phys. Rev. Lett. **98**, 131101 (2007).
[64] M. B. Wan, K. J. Jin, and W. M. Suen, arXiv:0807.1710.